7. K. A. Howard, D. E. Wilhelms, D. H. Scott, *Rev. Geophys. Space Phys.* **12**, 309–327 (1974).
8. T. H. Sweetser, M. S. Wallace, S. J. Hatch, R. B. Roncoli, Design of an Extended Mission for GRAIL, in *AIAA Astrodynamics Specialist Conference* (Minneapolis, MN, 2012) (2012), 18 pp.
9. Materials and methods are available as supplementary materials on *Science* Online.
10. D. D. Rowlands, R. D. Ray, D. S. Chinn, F. G. Lemoine, *J. Geod.* **76**, 307–316 (2002).
11. F. G. Lemoine *et al.*, *Geophys. Res. Lett.* **41**, 3382–3389 (2014).
12. D. E. Smith *et al.*, *Icarus* 10.1016/j.icarus.2016.06.006 (2016).
13. D. E. Smith *et al.*, *Space Sci. Rev.* **150**, 209–241 (2010).
14. M. T. Zuber *et al.*, *Science* **339**, 668–671 (2013).
15. Y. N. Kattoum, J. C. Andrews-Hanna, *Icarus* **226**, 694–707 (2013).
16. B. C. Johnson *et al.*, *Science* **354**, 441–444 (2016).
17. J. W. Head, in *Impact and Explosion Cratering*, D. J. Roddy, R. O. Pepin, R. B. Merrill, Eds. (Pergamon Press, New York, NY, 1977), pp. 563–573.
18. C. A. Hodges, D. E. Wilhelms, *Icarus* **34**, 294–323 (1978).
19. J. W. Head, *Geophys. Res. Lett.* **37**, L02203 (2010).
20. M. A. Wieczorek *et al.*, *Science* **339**, 671–675 (2013).
21. M. A. Wieczorek, R. J. Phillips, *Icarus* **139**, 246–259 (1999).
22. M. A. Wieczorek *et al.*, *Rev. Mineral. Geochem.* **60**, 221–364 (2006).
23. M. Xie, M.-H. Zhu, *Earth Planet. Sci. Lett.* **440**, 71–80 (2016).
24. J. Besserer *et al.*, *Geophys. Res. Lett.* **41**, 5771–5777 (2014).
25. W. S. Kiefer, R. J. Macke, D. T. Britt, A. J. Irving, G. J. Consolmagno, *Geophys. Res. Lett.* **39**, L07201 (2012).
26. M. T. Zuber, D. E. Smith, F. G. Lemoine, G. A. Neumann, *Science* **266**, 1839–1843 (1994).
27. G. A. Neumann, M. T. Zuber, D. E. Smith, F. G. Lemoine, *J. Geophys. Res.* **101**, 16841–16863 (1996).
28. A. S. Konopliv *et al.*, *Science* **281**, 1476–1480 (1998).
29. N. Namiki *et al.*, *Science* **323**, 900–905 (2009).
30. P. M. Muller, W. L. Sjogren, *Science* **161**, 680–684 (1968).
31. J. C. Andrews-Hanna, *Icarus* **222**, 159–168 (2013).
32. H. J. Melosh *et al.*, *Science* **340**, 1552–1555 (2013).
33. R. M. Schmidt, K. R. Housen, *Int. J. Impact Eng.* **5**, 543–560 (1987).
34. B. A. Ivanov, H. J. Melosh, E. Pierazzo, in *Large Meteorite Impacts and Planetary Evolution*, R. L. Gibson, W. U. Reimold, Eds. (Geological Society of America, Boulder, CO, 2010), pp. 29–49.
35. R. W. K. Potter, D. A. Kring, G. S. Collins, W. S. Kiefer, P. J. McGovern, *J. Geophys. Res.* **118**, 1–17 (2013).
36. R. W. K. Potter, D. Kring, G. S. Collins, W. S. Kiefer, P. J. McGovern, *Geophys. Res. Lett.* **39**, L18203 (2012).
37. G. A. Neumann *et al.*, *Sci. Adv.* **1**, e1500852 (2015).
38. A. Nahm, T. Öhman, D. Kring, *J. Geophys. Res.* **118**, 190–205 (2013).
39. J. F. McCauley, *Phys. Earth Planet. Inter.* **15**, 220–250 (1977).
40. S. P. S. Gulick *et al.*, *Rev. Geophys. Space Phys.* **51**, 31–52 (2013).



## ACKNOWLEDGMENTS

The GRAIL mission is supported by NASA's Discovery Program and is performed under contract to the Massachusetts Institute of Technology and the Jet Propulsion Laboratory. Topography was obtained from the Lunar Orbiter Laser Altimeter on the Lunar Reconnaissance Mission, managed by NASA's Goddard Space Flight Center. The NASA Pleiades and Center for Climate Simulation supercomputers were used to compute the gravity solutions. All data used in this study are archived in the Geosciences Node of the NASA Planetary Data System at http://geo.pds.nasa.gov/missions/grail/default.htm.


## SUPPLEMENTARY MATERIALS

www.sciencemag.org/content/354/6311/438/suppl/DC1
Materials and Methods
Supplementary Text
Figs. S1 to S8
References (*41*–*75*)

5 May 2016; accepted 16 September 2016
10.1126/science.aag0519

IMPACT CRATERS

# Formation of the Orientale lunar multiring basin

**Brandon C. Johnson,[1]*† David M. Blair,[2] Gareth S. Collins,[3] H. Jay Melosh,[4] Andrew M. Freed,[4] G. Jeffrey Taylor,[5] James W. Head,[6] Mark A. Wieczorek,[7] Jeffrey C. Andrews-Hanna,[8] Francis Nimmo,[9] James T. Keane,[10] Katarina Miljković,[1]‡ Jason M. Soderblom,[1] Maria T. Zuber[1]**

**Multiring basins, large impact craters characterized by multiple concentric topographic rings, dominate the stratigraphy, tectonics, and crustal structure of the Moon. Using a hydrocode, we simulated the formation of the Orientale multiring basin, producing a subsurface structure consistent with high-resolution gravity data from the Gravity Recovery and Interior Laboratory (GRAIL) spacecraft. The simulated impact produced a transient crater, ~390 kilometers in diameter, that was not maintained because of subsequent gravitational collapse. Our simulations indicate that the flow of warm weak material at depth was crucial to the formation of the basin's outer rings, which are large normal faults that formed at different times during the collapse stage. The key parameters controlling ring location and spacing are impactor diameter and lunar thermal gradients.**

Orientale, the youngest and best-preserved lunar multiring basin, exhibits three concentric topographic rings and an Inner Depression (*1*). The Inner Depression is a central topographic low associated with the zone of excavated crust that extends to a radial distance $R$ = 160 km from the basin center and is bounded by a scarp (*2*, *3*). The Outer Rook ($R \approx 330$ km) and Cordillera ($R \approx 430$ km) rings are topographically consistent with fault scarps (*3*, *4*). High-resolution gravity data from the Gravity Recovery and Interior Laboratory (GRAIL) spacecraft reveal that the Outer Rook and Cordillera rings are associated with offsets at the crust-mantle interface and localized zones of crustal thinning (*2*). The Inner Rook ($R \approx$ 230 km) is distinct, with a topographic signature similar to those of the peak rings of smaller basins (*3*, *5*) and is associated with a flattening of relief at the crust-mantle boundary (*2*).

To understand the processes that produced the subsurface structure inferred from gravity (*2*), we modeled the formation of Orientale using the two-dimensional version of iSALE, a multimaterial, multirheology, finite-difference shock physics code (*6*–*8*). Because iSALE is a continuum model, faults are manifest as localized regions of high strain rather than as discrete slip planes. Previous models of Orientale-scale impacts (*9*, *10*) showed subtle strain localization in the crust around the crater, hinting at ring fault formation during crater collapse, but were unable to resolve fault offsets (i.e., the amount of slip along the fault) and topographic expression. Below, we describe several model improvements that allowed us to directly resolve the formation of Orientale's rings and faults with kilometers of offset, in a manner not achievable with previous basin formation models (*9*–*13*). We include a dilatancy model (*14*), which describes how deformation increases the porosity of geological materials and contributes to shear localization (*15*). We use a damage model with an exponential dependence on strain (*15*), which results in more localized deformation in rocks that are already heavily fractured. For structures the size of Orientale, the curvature of the Moon's surface is important (*16*), so we model impacts into a spherical Moon-like target with a realistic central gravity field (*17*).

We assume a vertical impact of an asteroid made of dunite at a typical lunar impact velocity of 15 km/s (*18*). Our axisymmetric models have a spatial resolution of 1 km. We vary the impactor diameter, pre-impact crustal thickness, and thermal structure while attempting to match ring locations as well as the crustal thickness, which is derived from GRAIL gravity measurements and topography from the Lunar Orbiter Laser Altimeter (LOLA) on the Lunar Reconnaissance Orbiter (*19*, *20*). Because rock strength decreases as the melting temperature is approached (*7*), the assumed pre-impact thermal structure of the target body has the most

[1]Department of Earth, Atmospheric and Planetary Sciences, Massachusetts Institute of Technology, Cambridge, MA 02139, USA. [2]Massachusetts Institute of Technology Haystack Observatory, Route 40, Westford, MA 01886, USA. [3]Impacts and Astromaterials Research Centre, Department of Earth Science and Engineering, Imperial College London, London SW7 2AZ, UK. [4]Department of Earth, Atmospheric, and Planetary Sciences, Purdue University, West Lafayette, IN 47907, USA. [5]Hawai'i Institute of Geophysics and Planetology, University of Hawai'i, Honolulu, HI 96822, USA. [6]Department of Earth, Environmental and Planetary Sciences, Brown University, Providence, RI 02912, USA. [7]Institut de Physique du Globe de Paris, Sorbonne Paris Cité, Université Paris Diderot, Paris Cedex 13 75205, France. [8]Southwest Research Institute, Boulder, CO 80302, USA. [9]Department of Earth and Planetary Sciences, University of California, Santa Cruz, CA 95064, USA. [10]Department of Planetary Science, Lunar and Planetary Laboratory, University of Arizona, Tucson, AZ 85721, USA.
***Corresponding author. Email: brandon_johnson@brown.edu**
†Present address: Department of Earth, Environmental and Planetary Sciences, Brown University, Providence, RI 02912, USA.
‡Present address: Department of Applied Geology, Curtin University, Perth, WA 6102, Australia.

substantial effect on the formation of large impact basins (*9*–*12*, *16*, *21*). Our best-fitting model uses an impactor with a diameter of 64 km, a pre-impact crustal thickness of 52 km, and a linear thermal gradient of 14 K/km from a surface temperature of 300 K. The thermal structure transitions to an adiabat of ~0.04 K/km at temperatures exceeding 1300 K (fig. S1) and is consistent with the lunar thermal structure ~4 billion years ago (*17*, *21*).

Our model provides insight into the extent and temporal progression of excavation and crustal disruption, including the timing and formation of Orientale's rings (Fig. 1). The impact first produces a bowl-shaped crater with

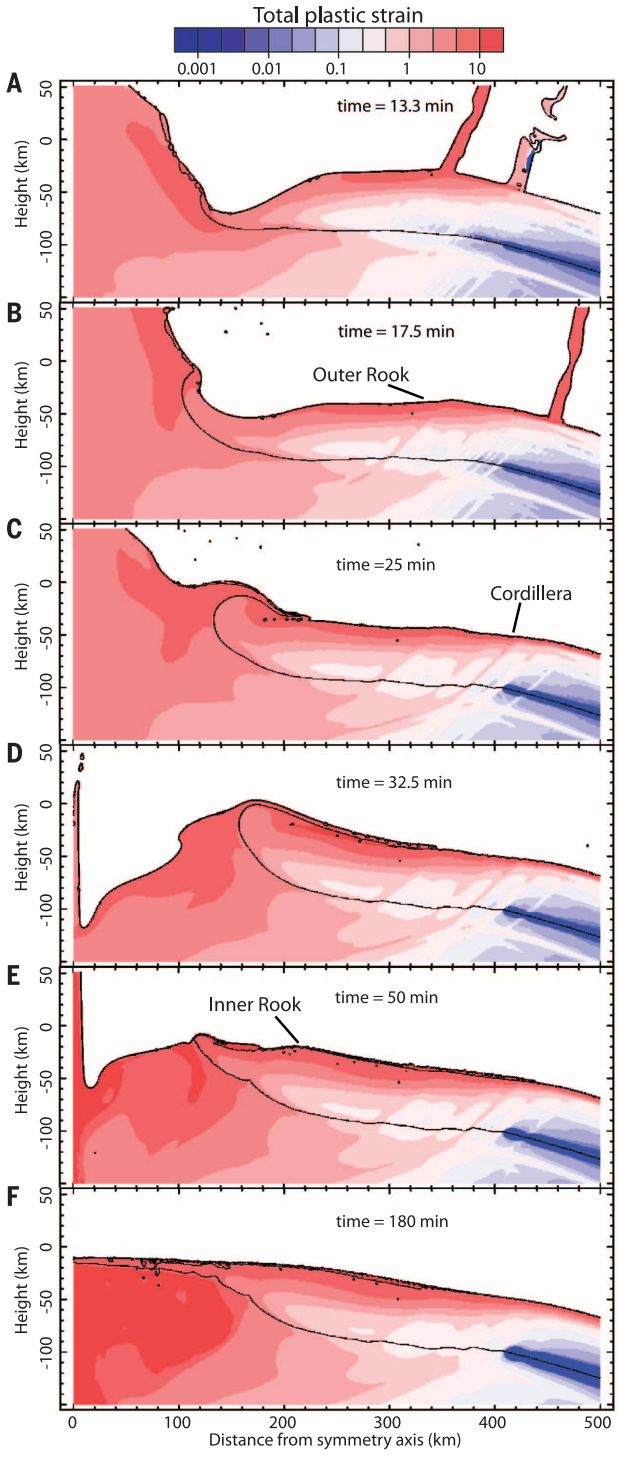


**Fig. 1. Time series for the best-fitting model of Orientale crater collapse and ring formation.** Material positions are colored according to their total plastic strain. The origin marks the point of impact. The thin black curves mark material interfaces (e.g., crust-mantle interface). Movie S1 is an animation of this figure.

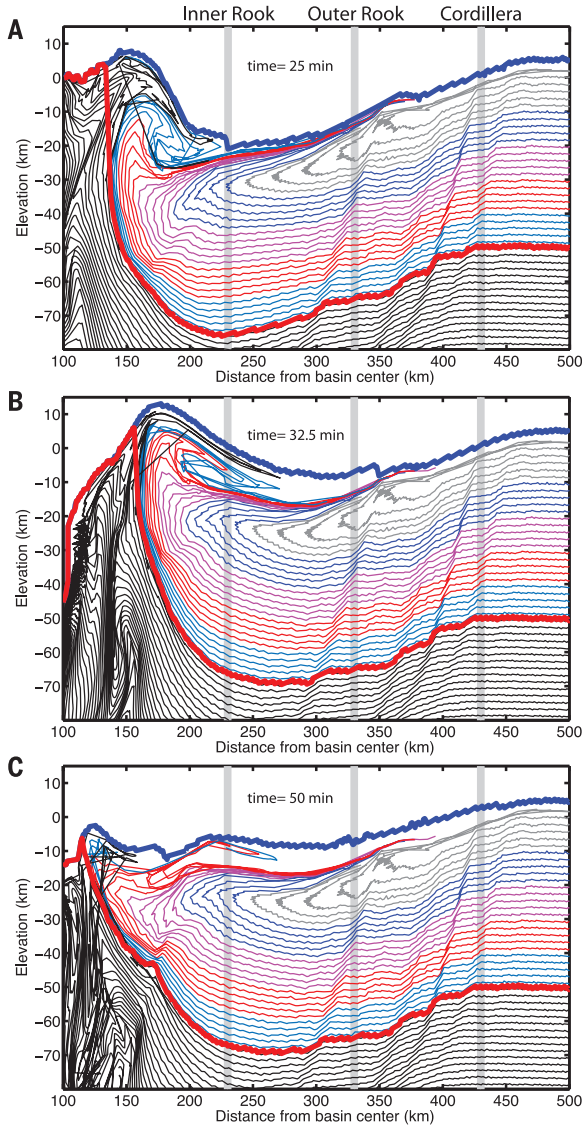


**Fig. 2. A vertically exaggerated time series of the formation of Orientale basin, highlighting the ring faults, formation of the Inner Rook, and material provenance.** Thin lines connect tracer particles, which track the motion of a parcel of material, that were initially at equal depths. Before the impact, these lines are parallel with a constant spacing of 2 km. Gray curves represent material from pre-impact depths of 0 to 10 km; dark blue, 10 to 20 km; magenta, 20 to 30 km; red, 30 to 40 km; blue, 40 to 50 km. The black curves represent mantle material. For clarity, lines are not drawn if the next nearest tracer is more than 50 km away. The upper thick blue and lower thick red curves mark model topography and the crust-mantle interface, respectively. The thick vertical gray lines mark the distance from the basin center where the present-day rings of Orientale are observed at the surface. Elevation and distance are with respect to a sphere, so that unperturbed material appears as a series of horizontal lines. This figure shows results for the best-fitting model.

a maximum depth of ~180 km; this cavity is unstable and experiences gravitational collapse. Although much of the deepest material collapses back into the crater, the maximum depth of excavation is ~55 km (i.e., into the mantle), where we define excavated material as any material on a ballistic trajectory and above the pre-impact surface at the time the crater has its maximum volume. Of the $5.7 \times 10^6$ km$^3$ of ejecta, $4.2 \times 10^6$ km$^3$ avoid collapsing into the crater and $1.2 \times 10^6$ km$^3$ are deposited between the basin rim and a distance of one basin diameter ($R$ = 430 to 860 km). These values are consistent with constraints from GRAIL and LOLA (*2*).

The time when the crater reaches its maximal volume is also used to determine the width of the transient crater ($R \approx 195$ km), which extends to a radial distance between the present-day Inner Depression and the Inner Rook ring and precedes the formation of any of the observed rings. Older studies have attempted to relate the rim of the transient crater to Orientale's rings (*1*, *22*–*26*), but the relative difference in their time of formation suggests that there is no reason to expect a correlation, and indeed no present-day topographic features correspond to the transient crater (*2*). This implies that for large impact basins, the transient crater and impactor size must be deduced not from topography but rather from the gravity and crustal thickness signature, using empirical relations from numerical models (*21*).

As the bowl-shaped transient crater collapses, a central uplift forms, composed of mantle material (Fig. 1A). As the crater continues to collapse, the Outer Rook fault (Fig. 1B) forms and ejecta are emplaced well outside the location where the Cordillera ring eventually forms after further inward collapse (Fig. 1C and Fig. 2A). This aspect of the simulation is consistent with observations suggesting that the Cordillera formed subsequent to ejecta emplacement (*3*). Our model predicts that both normal faults cut through the crust, and their dip angle (i.e., angle with respect to the surface) gradually decreases in the mantle (Fig. 1C and Fig. 2A). As illustrated in Fig. 2A, each fault has an offset of a few kilometers and has an average dip angle of 50° to 55° within the crust. Although the fault offsets are still present at late times, as evidenced by the displacement along tracer lines (Fig. 2C), numerical diffusion smooths the localized total plastic strain associated with the faults (Fig. 1, C and F).

The Outer Rook and Cordillera rings appear to be the scarps of large normal faults [e.g., (*1*, *3*)]. Our models indicate that these faults are the result of inward flow of warm, weak mantle material during collapse of the transient crater. This flow of weaker underlying material (Fig. 1 and fig. S2) pulls the cooler crust along with it, ultimately causing extensional faulting with large offsets far from the transient crater rim. In the best-fitting model, the strongest crustal material prior to the impact has a yield strength of 147 MPa and the weakest mantle material has a yield strength of 63 MPa (fig. S1). The role of the weak underlying mantle material is consistent with the ring tectonic theory of multi-ring basin formation (*24*).

After rising as high as 140 km above the surface, the central uplift collapses and produces a topographic bulge of crustal material ~10 km in height at $R \approx 175$ km (Fig. 2B). The formation of this bulge drives the development of the Inner Rook ring (Fig. 1D and Fig. 2B). This outcome of the simulation is consistent with earlier suggestions that the formation of the Inner Rook ring is analogous to the formation of peak rings observed in smaller basins (*5*, *9*). A secondary phase of inward collapse modifies the topographic expression of the Inner Rook (Fig. 1, D and E, and Fig. 2, B and C), perhaps distinguishing it from peak rings of smaller craters (*27*). Although the topographic signature of the Inner Rook is inconsistent with a fault scarp (*3*), the Inner Rook is associated with a local flattening of relief at the crust-mantle boundary (*2*), which is reproduced in our simulations (Fig. 2C). Our modeling predicts that the Inner Rook is composed of unmelted, lightly shocked crustal material from 35- to 40-km depths that is pushed over previously emplaced ejecta (Fig. 2 and figs. S3 and S4). This is consistent with observations indicating a cluster of localities composed of nearly pure crystalline plagioclase around the Inner Rook (*28*) and suggests that the crust around Orientale is nearly pure crystalline plagioclase even at depths exceeding 35 km, consistent with lunar bulk composition estimates (*29*).

In the hours after the impact, relatively cool (~1000 K) crustal material flows inward toward the basin center and covers the denser impact melt pool, which is dominated by mantle material (Fig. 1F and fig. S4). Combined with the fact that deeply excavated material collapses into the crater (Fig. 1A), this explains how a basin-scale impact that penetrates to mantle depths could contain crustal material at the basin center, as implied by crustal thickness models (*2*, *20*). Our models indicate that a thin deposit of crustal impact melt (fig. S5) covers the interior surface of Orientale, consistent with the morphologic and spectral interpretation of the Maunder formation (*30*). More oblique impacts, characterized by shallower excavation depths, would produce thicker crustal impact melt units (*11*).

Three hours after initial impact, the center of the basin is ~7 km deeper than currently observed (fig. S6). A deep post-impact basin is integral to the process that produces positive gravity anomalies over most lunar basins (*11*, *31*). Over the next few hundred million years, the basin center rises to its present position in response to the post-impact stress state (*11*, *31*). Mechanical coupling of the lithosphere in the basin center with the lithosphere associated with the crustal collar (annulus of thickest crust after transient crater collapse) enables the initially subisostatic basin center to uplift, becoming superisostatic and producing the free-air gravity anomaly of ~250 mGal (1 mGal = $10^{-5}$ m s$^{-2}$) over the center of Orientale (*11*, *31*, *32*).

Although our models do not result in a scarp bounding the Inner Depression ($R \approx 160$ km), they suggest that this scarp formed after the Inner Rook. Any topographic feature formed interior of $R \approx 200$ km, including the transient crater rim, would be destroyed by collapse of the central uplift (Fig. 1). After crater collapse, the impact melt pool extends from the basin center out to the edge of the Inner Depression (fig. S7). The Inner Depression is clearly associated with the mantle uplift (*2*). Although we cannot rule out formation of the scarp bounding the Inner Depression within a few hours of the impact, our modeling supports the inference that the Inner Depression formed on a much longer time scale, tectonically as the basin adjusted in response to the post-impact stress state (*11*, *33*), aided by cooling and contraction of Orientale's massive melt pool (*34*, *35*).

In our models, some mantle material splashes out onto the crust as the central uplift collapses (Fig. 1, C to F, and fig. S4), but this may be attributable to the limitations of our axisymmetric model. The southwestern quadrant of Orientale exhibits at least four large normal faults instead of two seen in other regions (*3*). The initial crustal thickness varies over the broad area of the Orientale basin; coupled with

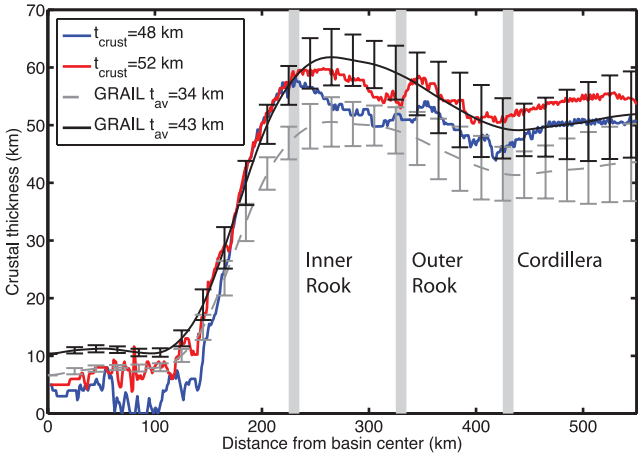


**Fig. 3. Post-impact crustal thickness.** The model thickness of the crust is plotted from the best-fitting model (red) and for a model with a pre-impact crustal thickness of 48 km (blue). Azimuthally averaged observed profiles of GRAIL-derived crustal thickness (*2*) are shown for comparison [global average crustal thickness $t_{av}$ = 43 km (black) and $t_{av}$ = 34 km (gray)]. Error bars are 1σ deviations from the mean.

the effects of an oblique impact, this may explain the marked difference between the development of rings in the eastern and western sectors of the basin.

In addition to forming rings in approximately the correct locations (Fig. 1 and fig. S8B), models with pre-impact crustal thicknesses that range from 48 to 52 km also reproduce the azimuthally averaged crustal thickness profile derived from GRAIL gravity and LOLA topography (Fig. 3). Our modeling shows that ring location and fault offsets are highly dependent on impactor size and the pre-impact thermal gradient (figs. S9 and S10). In our best-fitting model, the region where crust is thinned from the pre-impact value extends to $R_{thin} \approx 200$ km. The parameter $R_{thin}$ also provides an estimate for the radius of the zone of ejecta provenance or excavation cavity (*36*). In our best-fitting model of Orientale, these two metrics agree to within 5%. We favor the model with pre-impact crustal thickness of 52 km because it produces a thicker cap of cool crustal material at the center of the basin (Fig. 3), consistent with gravity observations.

Inverse models of GRAIL gravity data suggest that the Outer Rook and Cordillera are associated with localized crustal thinning and offsets at the crust-mantle interface (*2*). The crustal structure also reveals offsets at the crust-mantle interface that do not correlate with rings and may indicate additional subsurface faults. The faults with small offsets forming on either side of the Cordillera in our simulations may be consistent with these additional faults (Fig. 2). The amount of crustal thinning and magnitude of crust-mantle relief, however, depend on the assumptions of these inverse models (*2*). Our models exhibit local minima in the crustal thickness (Fig. 3) and offsets at the crust-mantle interface (Fig. 2) associated with the Outer Rook and Cordillera. These results are consistent with normal faults with offsets of a few kilometers cutting through the crust-mantle interface. The simple geometry of a normal fault with a dip angle of 50° and offset of 4 km cutting through 50-km-thick crust will create a ~40-km-wide region where the crust is thinned by ~3 km. This idealized fault geometry is similar to the modeled Outer Rook ring (Fig. 3, red curve 300 to 340 km from basin center). When extension occurs close to a fault (within ~40 km), the zone of crustal thinning is broader (Figs. 2 and 3 and fig. S8B). Inverse models of the crust-mantle interface are limited in resolution to a wavelength approximately equal to the crustal thickness. Thus, the predicted broader zone of extension may explain in part why the signature of the Cordillera is more robust than that of the Outer Rook (*2*). Similar local minima in crustal thickness as observed by GRAIL may reveal ring faults in highly degraded or mare-filled basins.

## REFERENCES AND NOTES


1. J. W. Head, *Moon* **11**, 327–356 (1974).
2. M. T. Zuber *et al.*, *Science* **354**, 438–441 (2016).
3. A. L. Nahm, T. Öhman, D. A. Kring, *J. Geophys. Res. Planets* **118**, 190–205 (2013).
4. Y. N. Kattoum, J. C. Andrews-Hanna, *Icarus* **226**, 694–707 (2013).
5. D. M. H. Baker *et al.*, *Icarus* **214**, 377–393 (2011).
6. A. A. Amsden, H. M. Ruppel, C. W. Hirt, *SALE: A Simplified ALE Computer Program for Fluid Flow at Speeds* (Los Alamos National Laboratories Report LA-8095, 1980).
7. G. S. Collins, H. J. Melosh, B. A. Ivanov, *Meteorit. Planet. Sci.* **39**, 217–231 (2004).
8. K. Wünnemann, G. S. Collins, H. J. Melosh, *Icarus* **180**, 514–527 (2006).
9. R. W. K. Potter, D. A. Kring, G. S. Collins, W. S. Kiefer, P. J. McGovern, *J. Geophys. Res. Planets* **118**, 963–979 (2013).
10. R. W. K. Potter, *Icarus* **261**, 91–99 (2015).
11. A. M. Freed *et al.*, *J. Geophys. Res. Planets* **119**, 2378–2397 (2014).
12. K. Miljković *et al.*, *Science* **342**, 724–726 (2013).
13. M.-H. Zhu, K. Wünnemann, R. W. K. Potter, *J. Geophys. Res. Planets* **120**, 2118–2134 (2015).
14. G. S. Collins, *J. Geophys. Res. Planets* **119**, 2600–2619 (2014).
15. L. G. J. Montési, *J. Geophys. Res.* **107** (B3), 2045 (2002).
16. B. A. Ivanov, H. J. Melosh, E. Pierazzo, *Geol. Soc. Spec. Pap.*, 29–49 (2010).
17. See supplementary materials on *Science* Online.
18. M. Le Feuvre, M. A. Wieczorek, *Icarus* **214**, 1–20 (2011).
19. D. E. Smith *et al.*, *Icarus* 10.1016/j.icarus.2016.06.006 (2016).
20. M. A. Wieczorek *et al.*, *Science* **339**, 671–675 (2013).
21. R. W. K. Potter, D. A. Kring, G. S. Collins, W. S. Kiefer, P. J. McGovern, *Geophys. Res. Lett.* **39**, L18203 (2012).
22. M. Laneuville, M. A. Wieczorek, D. Breuer, N. Tosi, *J. Geophys. Res. Planets* **118**, 1435–1452 (2013).
23. R. B. Baldwin, *Phys. Earth Planet. Inter.* **6**, 327–339 (1972).
24. H. J. Melosh, W. B. McKinnon, *Geophys. Res. Lett.* **5**, 985–988 (1978).
25. J. W. Head, *Geophys. Res. Lett.* **37**, L02203 (2010).
26. C. A. Hodges, D. E. Wilhelms, *Icarus* **34**, 294–323 (1978).
27. G. S. Collins, H. J. Melosh, J. V. Morgan, M. R. Warner, *Icarus* **157**, 24–33 (2002).
28. L. C. Cheek, K. L. Donaldson Hanna, C. M. Pieters, J. W. Head, J. L. Whitten, *J. Geophys. Res. Planets* **118**, 1805–1820 (2013).
29. G. J. Taylor, M. A. Wieczorek, *Philos. Trans. R. Soc. A* **372**, 20130242 (2014).
30. P. D. Spudis, D. J. P. Martin, G. Kramer, *J. Geophys. Res. Planets* **119**, 19–29 (2014).
31. H. J. Melosh *et al.*, *Science* **340**, 1552–1555 (2013).
32. M. T. Zuber *et al.*, *Science* **339**, 668–671 (2013).
33. P. K. Byrne *et al.*, *Earth Planet. Sci. Lett.* **427**, 183–190 (2015).
34. W. M. Vaughan, J. W. Head, L. Wilson, P. C. Hess, *Icarus* **223**, 749–765 (2013).
35. S. R. Bratt, S. C. Solomon, J. W. Head, *J. Geophys. Res.* **90**, 12415–12433 (1985).
36. M. A. Wieczorek, R. J. Phillips, *Icarus* **139**, 246–259 (1999).


## ACKNOWLEDGMENTS

We thank two anonymous reviewers for their thoughtful reviews; the developers of iSALE (www.isale-code.de/redmine/projects/iSALE), including K. Wünnemann, D. Elbeshausen, and B. Ivanov; and all those involved with the development and operations of the GRAIL spacecraft and the collection and reduction of the GRAIL data. This work was funded by the GRAIL mission, which is supported by the NASA Discovery Program and is performed under contract to the Massachusetts Institute of Technology and the Jet Propulsion Laboratory, California Institute of Technology. G.S.C. was funded by UK Science and Technology Facilities Council grant ST/N000803/1. At present, iSALE is not publicly available. It is distributed on a case-by-case basis to academic users in the impact community, strictly for noncommercial use. Scientists interested in using or developing iSALE should see www.isale-code.de/redmine/projects/isale/wiki/Terms_of_use for a description of application requirements. Model output has been published at the Harvard Dataverse, doi:10.7910/DVN/BH9UXW.

## SUPPLEMENTARY MATERIALS

www.sciencemag.org/content/354/6311/441/suppl/DC1
Materials and Methods
Figs. S1 to S10
Tables S1 and S2
Movie S1
References (*37*–*55*)

5 May 2016; accepted 8 September 2016
10.1126/science.aag0518

CHEMICAL KINETICS

# Direct frequency comb measurement of OD + CO → DOCO kinetics

**B. J. Bjork,[1]* T. Q. Bui,[1] O. H. Heckl,[1] P. B. Changala,[1] B. Spaun,[1] P. Heu,[2] D. Follman,[2] C. Deutsch,[3] G. D. Cole,[2,3] M. Aspelmeyer,[4] M. Okumura,[5] J. Ye[1]***

**The kinetics of the hydroxyl radical (OH) + carbon monoxide (CO) reaction, which is fundamental to both atmospheric and combustion chemistry, are complex because of the formation of the hydrocarboxyl radical (HOCO) intermediate. Despite extensive studies of this reaction, HOCO has not been observed under thermal reaction conditions. Exploiting the sensitive, broadband, and high-resolution capabilities of time-resolved cavity-enhanced direct frequency comb spectroscopy, we observed deuteroxyl radical (OD) + CO reaction kinetics and detected stabilized *trans*-DOCO, the deuterated analog of *trans*-HOCO. By simultaneously measuring the time-dependent concentrations of the *trans*-DOCO and OD species, we observed unambiguous low-pressure termolecular dependence of the reaction rate coefficients for $N_2$ and CO bath gases. These results confirm the HOCO formation mechanism and quantify its yield.**

The apparent simplicity of the gas-phase bimolecular reaction kinetics of free radicals often belies the complexity of the underlying dynamics. Reactions occur on multidimensional potential energy surfaces that can host multiple prereactive and bound intermediate complexes, as well as multiple transition states. As a result, effective bimolecular rate coefficients often exhibit complex temperature and pressure dependences. The importance of free radical reactions in processes such as combustion and air pollution chemistry has motivated efforts to determine these rate constants both experimentally and theoretically. Quantitative ab initio modeling of kinetics remains a major contemporary challenge (*1*), requiring accurate quantum chemical calculations of energies, frequencies, and anharmonicities; master equation

Editor's Summary

**titOn the origin of Orientale basinle**

Orientale basin is a major impact crater on the Moon, which is hard to see from Earth because it is right on the western edge of the lunar nearside. Relatively undisturbed by later events, Orientale serves as a prototype for understanding large impact craters throughout the solar system. Zuber *et al.* used the Gravity Recovery and Interior Laboratory (GRAIL) mission to map the gravitational field around the crater in great detail by flying the twin spacecraft as little as 2 km above the surface. Johnson *et al.* performed a sophisticated computer simulation of the impact and its subsequent evolution, designed to match the data from GRAIL. Together, these studies reveal how major impacts affect the lunar surface and will aid our understanding of other impacts on rocky planets and moons.

*Science*, this issue pp. 438 and 441